KAPL-P-000160
(K97041)
CONF-970922--

A NEW MECHANISTIC MODEL OF CRITICAL HEAT FLUX IN FORCED-CONVECTION SUBCOOLED BOILING

A. Alajbegovic, (S. D'Amico)

October 1997

NOTICE

KAPL ATOMIC POWER LABORATORY SCHENECTADY, NEW YORK 10701

Operated for the U. S. Department of Energy
by KAPL, Inc. a Lockheed Martin company

DISCLAIMER

A NEW MECHANISTIC MODEL OF CRITICAL HEAT FLUX IN FORCED-CONVECTION SUBCOOLED BOILING

A. Alajbegovic, N. Kurul, M.Z. Podowski, D.A. Drew and R.T. Lahey, Jr.
Center for Multiphase Research
Rensselaer Polytechnic Institute
Troy, New york 12180-3590, USA

1. INTRODUCTION

Because of its practical importance and various industrial applications, the process of subcooled flow boiling has attracted a lot of attention in the research community in the past. However, the existing models are primarily phenomenological and are based on correlating experimental data rather than on a first-principle analysis of the governing physical phenomena. Even though the mechanisms leading to critical heat flux (CHF) are very complex, the recent progress in our understanding of local phenomena of multiphase flow and heat transfer, combined with the development of mathematical models and advanced Computational Fluid Dynamics (CFD) methods, makes analytical predictions of CHF quite feasible. The purpose of this paper is to present a new mechanistic model of CHF in boiling channels under subcooled boiling conditions.

The main characteristic of forced-convection subcooled boiling is that it results in very effective heat transfer driven by local evaporation and condensation phenomena under thermodynamic nonequilibrium conditions. The total wall heat flux can be partitioned into the contribution due to nucleate boiling and the heat transfer rate due to evaporation from the thin liquid sublayer beneath large bubbles formed near the wall. It has been observed that the very efficient heat transfer by nucleate boiling may be severely reduced by the evaporation of the microlayer. This may lead to local dryout and wall temperature excursion, the situation known as departure from nucleate boiling (DNB) or critical heat flux (CHF). The thickness of the sublayer corresponds to that of the viscous sublayer. Large bubbles are being formed through the combined effects of coalescence and evaporation. They slide along the liquid sublayer, and their length is important for dryout. Based on existing experimental evidence, bubble length can be approximated by the critical wavelength of the Helmholtz vapor/liquid interface instability. Another possible cause for dryout of the sublayer occurs at high evaporation rates in the nucleate boiling region. The increased bubble concentration possibly combined with interfacial instability may effectively prevent replenish-

ment of the liquid into the sublayer. This effect depends on the size of nucleated bubbles.

The most important effects which lead to dryout and critical heat flux (CHF) can be summarized as:

- dryout of the sublayer beneath large bubbles accumulated along the channel wall, and
- dryout of the sublayer due to prevention of sublayer replenishment in the nucleate boiling region.

The most important parameters for the quantification of these effects are:

- sublayer thickness and evaporation rate,
- the length of large bubbles,
- the evaporation rate in the nucleate boiling region, and
- the bubble diameter on departure from the nucleation site.

A detailed model of the phenomena which may lead to the dryout is presented in the next section.

2. MODEL FORMULATION

One of the most important mechanisms for the bubble growth in subcooled boiling is the evaporation from the liquid microlayer beneath the vapor bubbles. The thickness of this microlayer can vary [1]. If the microlayer is larger than the size of the node next to the wall, its effect is captured automatically using the overall CFD model. However, the bubbles moving very close to the wall may slide on the viscous sublayer. The thickness of this layer is much too small to be taken into account by any CFD scheme. For various reasons, the size of the nodes next to the wall must be specified to be much larger than the viscous sublayer thickness. Therefore, wall heat partitioning must be implemented as a boundary condition.

2.1. Evaluation of Wall Temperature

For each of the regions shown in Figure 1, the energy balance for the wall can be written. Using a "thin wall" assumption, the thickness-averaged time-dependent wall temperature can be expressed as

$$T_{wi} = \frac{1}{t_1 - t_0} \int_{t_{i-1}}^{t_i} T_w(\tau) d\tau \tag{1}$$

for $i=1,2,3$, where, $t_1 - t_0$, $t_2 - t_1$ and $t_3 - t_2$, respectively, are the passage times of Regions I, II and III, respectively.

The average wall temperature can be expressed as

$$\bar{T}_w = \frac{(t_1 - t_0)T_{w1} + (t_2 - t_1)T_{w2} + (t_3 - t_2)T_{w3}}{t_3 - t_0} \tag{2}$$

The time intervals in the above equation can be obtained from the known near-wall flow structure. In particular, the relative time of the large bubble's passage is

$$\alpha_{wLB} = \frac{(t_2 - t_0)}{(t_3 - t_0)} \tag{3}$$

Also, we can relate the dryout time during the large bubble's passage to the overall time of the large bubble passage by introducing a parameter

$$a = \frac{(t_2 - t_1)}{(t_2 - t_0)} \tag{4}$$

The wall temperature as a function of time for each of the regions shown in Figure 1 can be evaluated from the respective energy balances. Specifically, for Region-I we have

$$c_{ps}\rho_s L_{LB} \frac{d}{dt} T_{w1}(t) = q_w'' - \frac{k_l}{\delta(t)}(T_{w1}(t) - T_{sat}) \tag{5}$$

where ρ_s and c_{ps} are the density and specific heat of the solid wall, L_{LB} is the length of large bubbles and $\delta(t)$ is the time-dependent thickness of the laminar sublayer between the long bubbles and the wall. The energy balance for the evaporating sublayer yields

$$-h_{fg}\rho_l \frac{d}{dt}\delta(t) = \frac{k_l}{\delta(t)}(T_{w1}(t) - T_{sat}) \tag{6}$$

The initial conditions for Eqs.(5) and (6) are:

$$T_{w1}(0) = T_{w01} \tag{7}$$

$$\delta(0) = \delta_0 \tag{8}$$

Combining Eqs.(5)-(8), yields the following expression for the wall temperature

$$T_{w1}(t) = \frac{1}{c_{ps}\rho_s L}[q''_w t + h_{fg}\rho_l(\delta(t) - \delta_0)] + T_{w01} \tag{9}$$

The change of sublayer thickness with time is needed for the determination of the wall temperature. The following nonlinear differential equation for the sublayer thickness is obtained by combining Eqs. (6) and (9)

$$A\delta'(t)\left(\frac{d}{dt}\delta'(t)\right) + B + \delta'(t) + t' - 1 = 0 \tag{10}$$

where

$$A = \frac{c_{ps}\rho_s L q''_w}{h_{fg}\rho_l k_l} \tag{11}$$

$$B = \frac{c_{ps}\rho_s L(T_{w01} - T_{sat})}{h_{fg}\rho_l \delta_0} \tag{12}$$

$$\delta'(t) = \frac{\delta(t)}{\delta_0} \tag{13}$$

$$t' = \frac{q''_w}{h_{fg}\rho_l \delta_0} t \tag{14}$$

For large A>>1 or B>>1, Eq.(10) becomes

$$A\delta'(t)\left(\frac{d}{dt}\delta'(t)\right)+B+t' = 0 \tag{15}$$

The solution of the above equation is

$$\delta'(t) = \sqrt{1-2\frac{B}{A}t'-\frac{1}{A}t'^2} \tag{16}$$

In the case where both A<<1 and B<<1, the solution can be approximated by

$$\delta'(t) = 1-t' \tag{17}$$

The solutions given by Eqs.(16) and (17) can be rewritten in dimensionalized form as

$$\delta(t) = \delta_0\sqrt{1-2\frac{k_l(T_{w01}-T_{sat})}{q''_w\delta_0}t-\frac{k_l q''_w}{c_{ps}\rho_s L h_{fg}\rho_l\delta_0^2}t^2} \qquad \text{for A>>1 or B>>1} \tag{18}$$

and

$$\delta(t) = \delta_0-\frac{q''_w}{h_{fg}\rho_l}t \qquad \text{for A<<1 and B<<1} \tag{19}$$

The energy balance for the wall in Region-II becomes

$$c_{ps}\rho_s L\frac{d}{dt}T_{w2}(t) = q''_w-H_v(T_{w2}(t)-T_{sat}) \tag{20}$$

where H_v is the vapor heat transfer coefficient.

Using the initial condition

$$T_{w2}(0) = T_{w02} \tag{21}$$

Eq.(20) can be solved for the wall temperature

$$T_{w2}(t) = T_{w02}e^{-\frac{H_v}{c_{ps}\rho_s L}t} + \left(T_{sat} + \frac{q''_w}{H_v}\right)\left(1 - e^{-\frac{H_v}{c_{ps}\rho_s L}t}\right) \tag{22}$$

For Region-III we write

$$c_{ps}\rho_s L\frac{d}{dt}T_{w3}(t) = q''_w - H_c(T_{w3}(t) - T_l) - q''_B \tag{23}$$

where H_c is the liquid heat transfer coefficient and q''_B is the boiling component of the heat transfer rate in subcooled boiling.

The solution with the initial condition

$$T_{w3}(0) = T_{w03} \tag{24}$$

can be written as

$$T_{w3}(t) = T_{w03}e^{-\frac{H_c}{c_{ps}\rho_s L}t} + \left(T_l + \frac{q''_w - q''_B}{H_c}\right)\left(1 - e^{-\frac{H_c}{c_{ps}\rho_s L}t}\right) \tag{25}$$

The mean wall temperature can be calculated using Eq.(2). First, however, time instants t_1, t_2 and t_3 must be obtained relative to t_0. By knowing the mean length of large bubbles (or slugs) in the flow direction and their velocity, the following expression is obtained

$$t_2 - t_0 = \frac{L_{LB}}{v_{LB}} \tag{26}$$

where v_{LB} is the velocity of large bubbles.

Eq.(3) yields

$$t_3 - t_0 = \frac{t_2 - t_0}{\alpha_{wLB}} = \frac{L_{LB}}{\alpha_{wLB}v_{LB}} \tag{27}$$

and

$$t_3 - t_2 = \left(\frac{1-\alpha_{wLB}}{\alpha_{wLB}}\right)(t_2 - t_0) = \left(\frac{1-\alpha_{wLB}}{\alpha_{wLB}}\right)\frac{L_{LB}}{v_{LB}} \tag{28}$$

The interval t_1-t_0 is the time needed for the complete evaporation of the sublayer beneath the large bubbles, and it can be calculated from Eqs.(18) or (18) by taking $\delta(t_1) = 0$. Naturally, the length of this should not exceed the passage interval of the large bubbles, t_2-t_0.

Using the solution from the previous section, the wall temperature at the end of each time interval becomes

$$T_w(t_1) = A_1 + T_{w0,1} \tag{29}$$

$$T_w(t_2) = A_2 T_{w0,2} + B_2 \tag{30}$$

$$T_w(t_3) = A_3 T_{w0,3} + B_3 \tag{31}$$

where

$$T_{w0,1} = T_w(t_3) \tag{32}$$

$$T_{w0,2} = T_w(t_1) \tag{33}$$

$$T_{w0,3} = T_w(t_2) \tag{34}$$

and

$$A_1 = \frac{1}{c_{ps}\rho_s L}[q''_w t_1 + h_{fg}\rho_l(\delta(t_1) - \delta_0)] \tag{35}$$

$$A_2 = e^{-\frac{H_v}{c_{ps}\rho_s L}(t_2 - t_1)} \tag{36}$$

$$A_3 = e^{-\frac{H_c}{c_{ps}\rho_s L_{LB}}(t_3 - t_2)} \tag{37}$$

$$B_2 = \left(T_{sat} + \frac{q''_w}{H_v}\right)\left(1 - e^{-\frac{H_v}{c_{ps}\rho_s L_{LB}}(t_2 - t_1)}\right) \tag{38}$$

$$B_3 = \left(T_l + \frac{q''_w - q''_B}{H_v}\right)\left(1 - e^{-\frac{H_c}{c_{ps}\rho_s L_{LB}}(t_3 - t_2)}\right) \tag{39}$$

Solving the above equations gives the solution for the initial wall temperature in each region:

$$T_{w0,1} = \frac{A_1 A_2 A_3 + A_3 B_2 + B_3}{1 - A_2 A_3} \tag{40}$$

$$T_{w0,2} = \frac{A_1 + A_3 B_2 + B_3}{1 - A_2 A_3} \tag{41}$$

$$T_{w0,1} = \frac{A_1 A_2 + A_2 B_3 + B_2}{1 - A_2 A_3} \tag{42}$$

By knowing these values one can also obtain the time-dependent wall temperature in each region shown in Figure 1. Then, the mean overall wall temperature can be evaluated.

We consider the case with both A<<1and B<<1 for Region-I. Combining Eqs.(9) and (19) with Eq.(1) yields

$$\bar{T}_{w1} = \frac{1}{t_1 - t_0}\int_{t_0}^{t_1} T_w(t)dt = T_{w01} \tag{43}$$

From Eq.(22) we have

$$\bar{T}_{w2} = \frac{1}{t_2 - t_1}\int_{t_1}^{t_2} T_w(t)dt = \tag{44}$$

$$\left(T_{sat} + \frac{q''_w}{H_v}\right) + \frac{c_{ps}\rho_s L_{LB}}{H_v}\frac{\left(T_{w02} - T_{sat} - \frac{q''_w}{H_v}\right)}{(t_2 - t_1)}\left(e^{-\frac{H_v}{c_{ps}\rho_s L_{LB}}t_1} - e^{-\frac{H}{c_{ps}\rho_s L_{LB}}t_2}\right)$$

Similarly, from Eq.(25) we obtain

$$\bar{T}_{w3} = \frac{1}{t_3 - t_2}\int_{t_2}^{t_3} T_w(t)dt = \tag{45}$$

$$\left(T_c + \frac{q''_w - q''_B}{H_c}\right) + \frac{c_{ps}\rho_s L_{LB}}{H_c}\frac{\left(T_{w03} - T_l - \frac{q''_w - q''_B}{H_c}\right)}{(t_3 - t_2)}\left(e^{-\frac{H_v}{c_{ps}\rho_s L_{LB}}t_2} - e^{-\frac{H_v}{c_{ps}\rho_s L_{LB}}t_3}\right)$$

Eqs.(43)-(45) can now be substituted into Eq.(2) to obtain the overall mean wall temperature.

2.2. The Model of Large Bubble

The length of large bubbles has been measured by Galloway & Mudawar [2] and Gersey & Mudawar [3] and was found to agree very well with the critical wavelength of the Helmholtz instability at the vapor/liquid interface. Comparing the pressure drop at the wavy interface calculated from the kinematic considerations to that due to surface tension yields the following expression for the critical wavelength in vertical flows

$$k_c = \frac{2\pi}{\lambda_c} = \frac{\rho''_l \rho''_v (v_v - v_l)^2}{\sigma(\rho''_l + \rho''_v)} \tag{46}$$

where

$$\rho''_l = \rho_l \coth(k\Delta_l) \tag{47}$$

$$\rho''_v = \rho_v \coth(k\Delta_v) \tag{48}$$

and Δ_v and Δ_l, are the distances between the interface and the walls in the vapor and liquid regions, respectively.

Therefore, the length of a large bubble has been calculated as

$$L_{LB} = \lambda_c = \frac{2\pi\sigma(\rho''_l + \rho''_v)}{\rho''_l \rho''_v (v_v - v_l)^2} \tag{49}$$

Another parameter of interest to the present model is the distance between the elongated bubbles and the wall, corresponding to the viscous sublayer [4]. The thickness of the viscous sublayer can be evaluated from

$$\delta_0 = \frac{10\nu}{u_\tau} \tag{50}$$

where $u_\tau = \sqrt{\tau_w / \rho_l}$ is the shear velocity.

If the supply of liquid to the sublayer is interrupted, the sublayer cannot be restored after the large bubble's passage. Therefore, in that case the initial sublayer thickness becomes zero. Again, we can use Helmholtz instability to calculate the case when the liquid can no longer replenish the liquid sublayer.

The critical velocity for this case can be obtained from Eq.(49) by replacing ρ''_l by ρ_l and ρ''_v by ρ_v, and using the diameter of small bubbles instead of the length of large bubbles. The result becomes

$$u_{max} = |u_l - u_g| = \sqrt{\frac{2\pi\sigma(\rho_l + \rho_v)}{\rho_l \rho_v D_B}} \tag{51}$$

The vapor velocity can be obtained from

$$u_g = \frac{q''_w}{\rho_v h_{fg}} \frac{A_g}{A_w} \tag{52}$$

where A_g is the wall area beneath the large bubble covered by vapor jets. The liquid velocity is obtained using the mass conservation,

$$u_l = -u_g \frac{\rho_v}{\rho_l} \frac{A_g}{A_w - A_g} \tag{53}$$

2.3. Model Closure

In order to achieve closure of the overall CHF model, several additional phenomena must be accounted for. These include, but are not limited to: nucleation frequency, nucleation site density, bubble diameter at departure, and interfacial heat transfer coefficient. The necessary closure laws can be found in Ref. [5]

3. RESULTS AND DISCUSSION

As discussed in the previous section, using the following parameters as input: liquid subcooling, liquid velocity and void fraction in the next-to-wall node, the proposed model evaluates the mode(s) of heat transfer and the wall temperature. If the actual heat flux is above the critical heat flux at these conditions, an excursion in the wall temperature would result. This can be illustrated by evaluating the wall temperature for various values of the next-to-wall node parameters mentioned above. In Figs. 2 and 3, the estimated wall temperature is plotted for a range of liquid subcoolings and void fractions for two different liquid velocities for heat flux of 190 kW/m^2 for Freon. The jump in the wall temperature can be clearly seen at high void fraction and low subcooling indicating that the heat flux in this range is above the critical heat flux. As expected, CHF is likely to occur at high local void fractions near the wall, and its likelihood increases with decreasing velocity and subcooling.

The model predictions have been compared against the experimental data of Hino & Ueda [6]. The test section was a vertical concentric annulus with the inner tube heated. The heated section contained a stainless-steel tube, 8 mm o.d., 400 mm long. The outer tube was made of pyrex tube, 18 mm i.d. The resultant hydraulic diameter was 10 mm. The fluid used in the experiment was Freon R-113 at a fixed pressure of 0.147 MPa (the corresponding saturation temperature was 332 K).

The results of calculations shown in Figures 4 through 8 and in Table 1 were obtained by incorporating the new CHF model into the overall model of a boiling channel and using the CFX 4 computer code as a numerical solver of the governing equations.

Figures 4 through 8 show the predictions for the case with 30 degrees subcooling and a low mass flux (G=512 kg/m^2-s). The heat flux used in these calculations was 190 kW/m^2. The temperature excursion at around 0.4 m. from inlet is clearly visible in Figure 4, which is the point of CHF. The axial distributions of the cross-section averaged void fraction and the superficial velocities of both liquid and vapor are shown in Figures 5 and 6. Also, the radial distributions of the temperature and local void fraction just before the CHF point are shown in Figures 7 and 8.

Table 1 gives a comparison between the experimental and the predicted values of the critical heat flux for various subcoolings for the same mass flux as shown in Figures 4 - 8. The results for a larger mass flux are shown in Table 2.

Tables 1 and 2 give the comparison of the experimental and predicted values of the critical heat flux.

Table 1: Predicted critical heat fluxes, $G = 512\ kg/m^2s$

ΔT_{sub} [K]	Measured [6] $[kW/m^2]$	Predicted $[kW/m^2]$	Relative error
30	241	190	-21%
20	211	160	-24%
10	174	125	-28%

Table 2: Predicted critical heat fluxes, $G = 1239 kg/m^2s$

ΔT_{sub} [K]	Measured [6] $[kW/m^2]$	Predicted $[kW/m^2]$	Relative error
30	332	405	+22%
20	277	302	+9%
10	244	170	-30%

As can be seen, the discrepancies between the predication and data are within the $\mp 30\,\%$ error bound. This result is consistent with the accuracy of experimental data for CHF. Furthermore, a sensitivity study which was performed has shown that adjusting the calculated nucleation frequency significantly improves the agreement between the predictions and the data. This points to the conclusion that a better model for the nucleation frequency is needed.

4. CONCLUSIONS

Various mechanisms leading to CHF in subcooled boiling have been investigated. A new model for the predictions of the onset of CHF has been developed. This new model has been coupled with the overall boiling channel model, numerically implemented in the CFX 4 computer code, tested and validated against the experimental data of Hino & Ueda [6]. The predicted critical heat flux for various channel operating conditions shows good agreement with the measurements using the aforementioned closure laws for the various local phenomena governing nucleation and bubble departure from the wall. The observed differences are consistent with typical uncertainties associated with CHF data [7].

ACKNOWLEDGEMENTS

The authors wish to express their gratitude to: D. Edwards, M. Erdman, C. Gersey and G. Kirouac, for their technical assistance and fruitful technical discussions.

REFERENCES

[1] I.A. Mudawar, T.A. Incropera and F.P. Incropera, "Boiling Heat Transfer and Critical Heat Flux in Liquid Films Falling on Vertically-Mounted Heat Sources," *Int. J. Heat Mass Transfer*, **30**, 2083-2095, 1987.

[2] J.E. Galloway and I. Mudawar, "CHF Mechanism in Flow Boiling From a Short Heated Wall-I. Examination of Near-Wall Conditions With the Aid of Photomicrography and High-Speed Video Imaging," *Int. J. Heat Mass Transfer*, **36**, 2511-2526, 1993.

[3] C.O. Gersey and I. Mudawar, "Effects of Heater Length and Orientation on the Trigger Mechanism for Near-Saturated Flow Boiling Critical Heat Flux- I. Photographic Study and Statistical Characterization of the Near-Wall Interfacial Features," *Int. J. Heat Mass Transfer*, **36**, 629-641, 1995.

[4] E. Moursali, J.L. Marie, J. Bataille, "An Upward Bubbly Boundary Layer Along a Vertical Flat Plate," *Int. J. Multiphase Flow*, **21**, 107-117, 1995.

[5] N. Kurul and M.Z. Podowski, "On The Modeling of Multidimensional Effects in Boiling Channels," ANS Proc. 27th National Heat Transfer Conference, Minneapolis, MN, July 28-31, 1991.

[6] R. Hino and T. Ueda, "Studies on Heat Transfer and Flow Characteristics in Subcooled Flow Boiling-Part 2. Flow Characteristics," *Int. J. Multiphase Flow*, **11**, 283-397, 1985.

[7] N.E. Todreas and M.S Kazimi, *Nuclear Systems I - Thermal Hydraulic Fundamentals*, Hemisphere Publishing Corp., 1991.

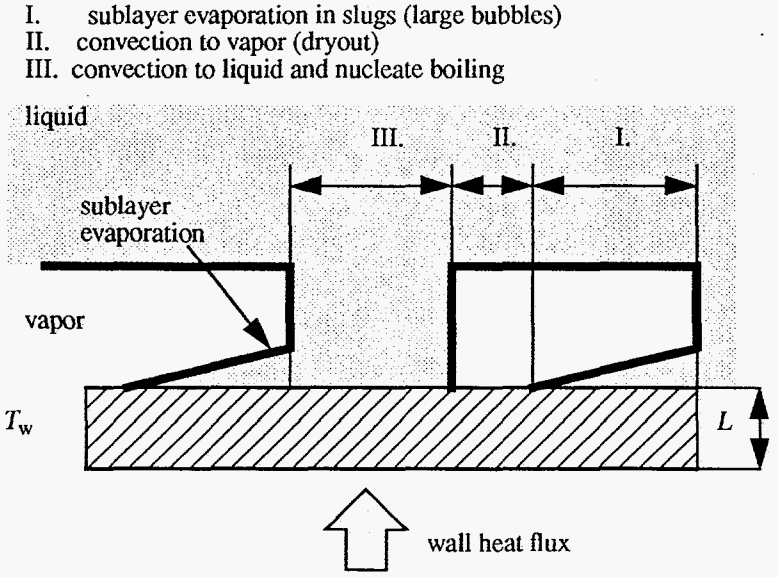

Figure 1. A schematic of structures important for the wall heat partitioning.

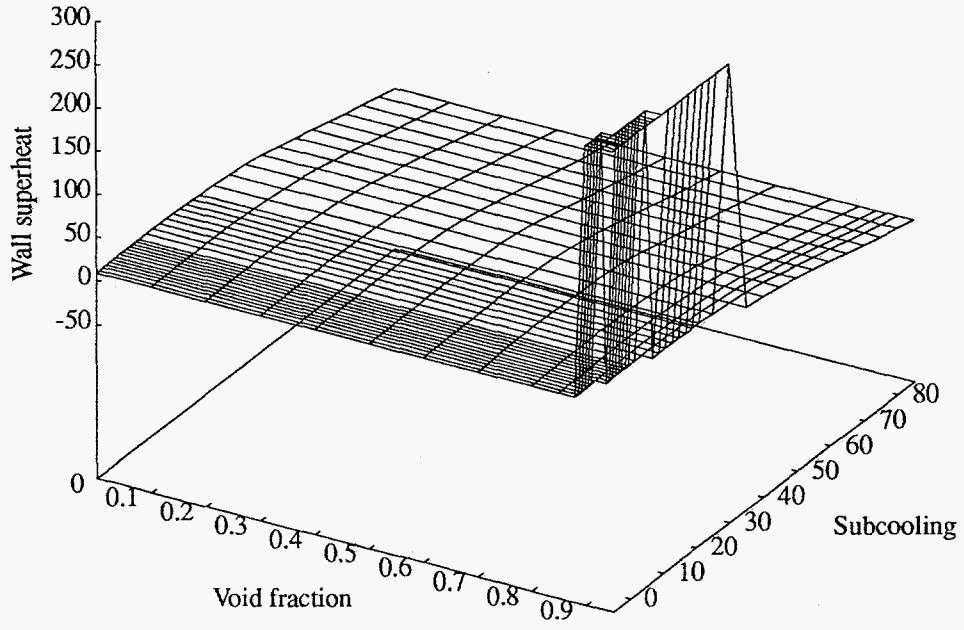

Figure 2. Predictions of critical heat flux for Freon at p = 1.5 bars, q"=190 kW/m^2 , at constant liquid velocity of 0.5 m/s

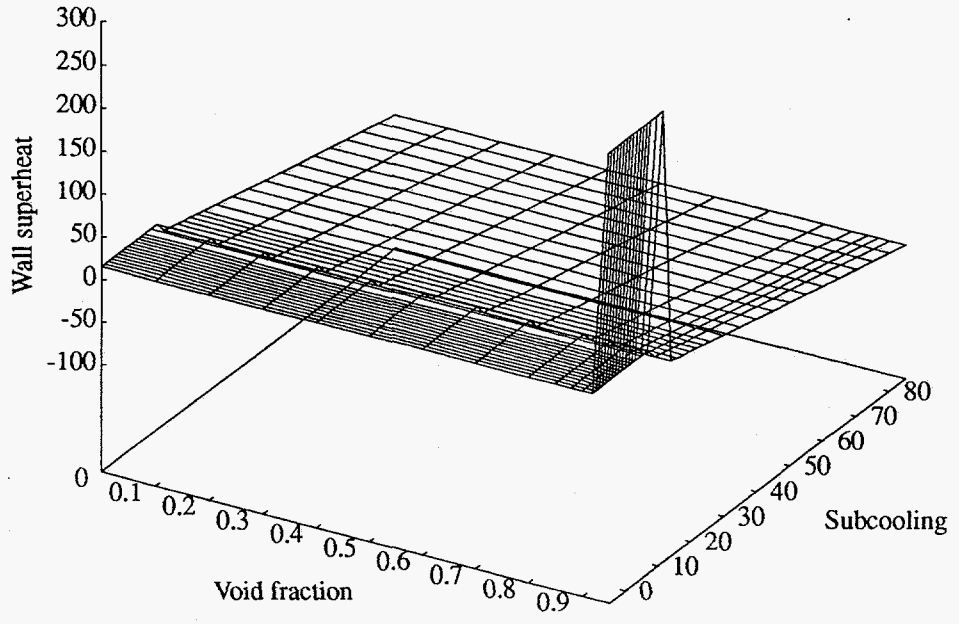

Figure 3. Predictions of critical heat flux for Freon at p = 1.5 bars, q"=190 kW/m^2 , at constant liquid velocity of 2.0 m/s

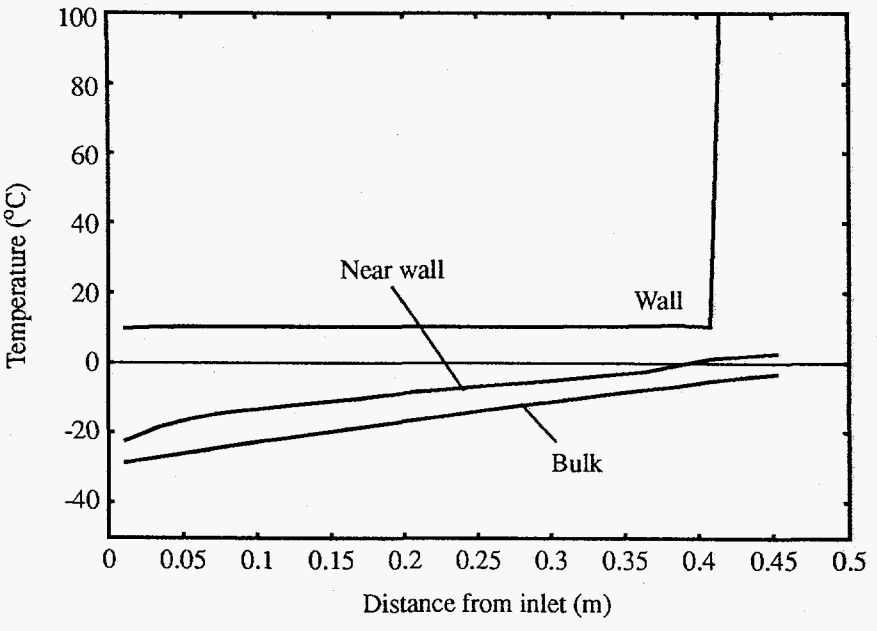

Figure 4. Axial Temperature Distributions obtained for the experimental data of Hino & Ueda [6], G=512 kg/s ΔT_{in}= 30 °C q"= 190 kW/m^2 p= 0.147 MPa.

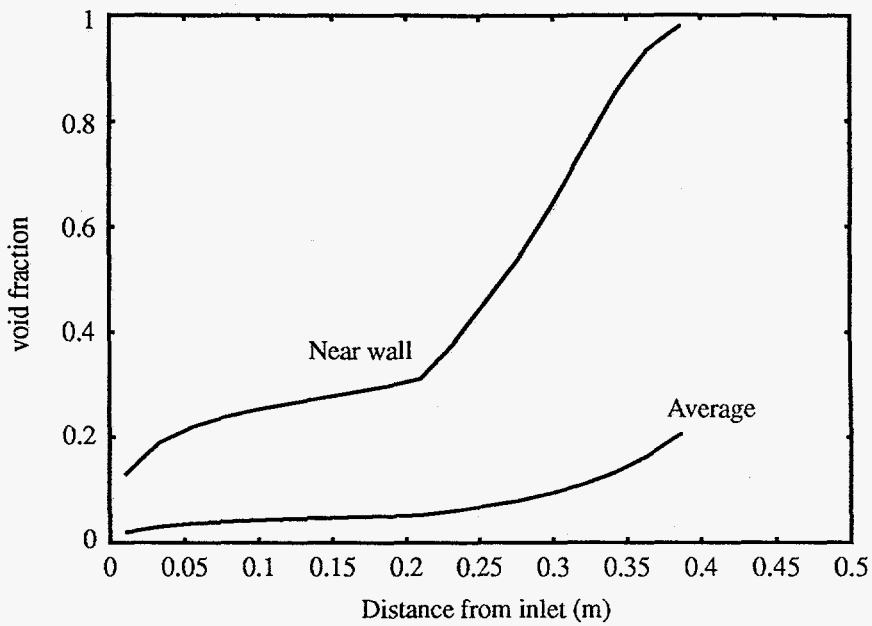

Figure 5. Axial void fraction distribution obtained for the experimental data of Hino & Ueda [6], G=512 kg/s ΔT_{in}= 30 °C q"= 190 kW/m^2 p= 0.147 MPa.

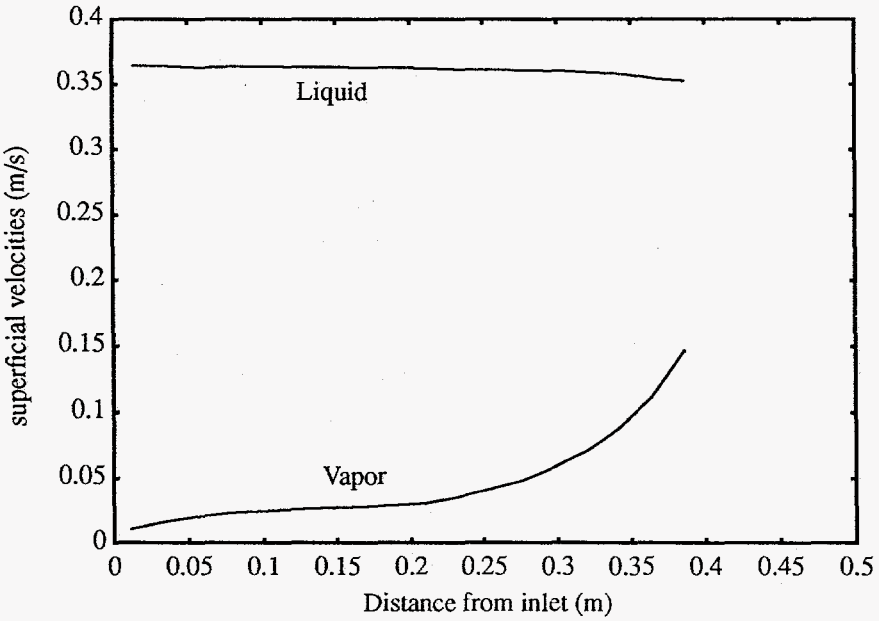

Figure 6. Axial superficial velocity distributions obtained for the experimental data of Hino & Ueda [6], G=512 kg/s ΔT_{in}= 30 °C q"= 190 kW/m^2 p= 0.147 MPa.

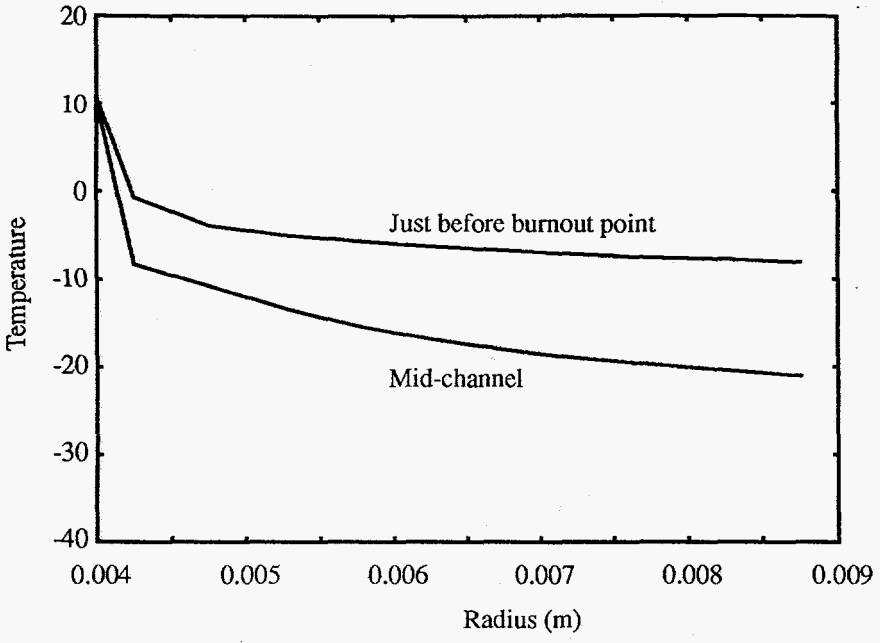

Figure 7. Radial temperature distribution obtained for the experimental data of Hino & Ueda [6], G=512 kg/s ΔT_{in}= 30 °C q"= 190 kW/m^2 p= 0.147 MPa.

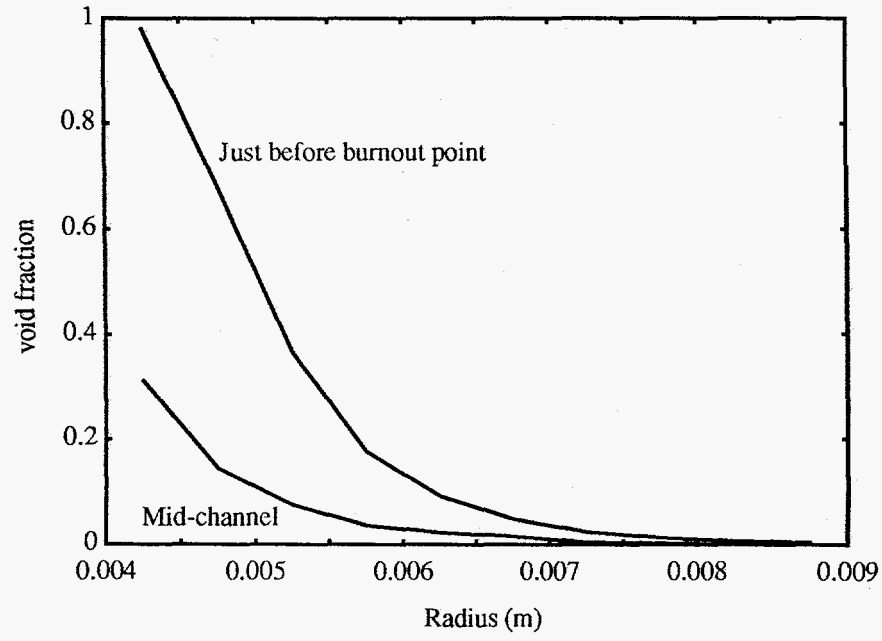

Figure 8. Radial void fraction distribution obtained for the experimental data of Hino & Ueda [6], G=512 kg/s ΔT_{in}= 30 °C q"= 190 kW/m^2 p= 0.147 MPa.